

## Probing the uniaxial strain-dependent valley drift and Berry curvature in monolayer MoSi<sub>2</sub>N<sub>4</sub>

Sajjan Sheoran <sup>\*</sup>, Manjari Jain, Ruman Moulik , and Saswata Bhattacharya <sup>†</sup>

*Department of Physics, Indian Institute of Technology Delhi, New Delhi 110016, India*



(Received 9 June 2023; accepted 18 October 2023; published 13 November 2023)

We use *ab initio* calculations and theoretical analysis to investigate the influence of uniaxial tensile strain on valley drifts and Berry curvatures in the monolayer MoSi<sub>2</sub>N<sub>4</sub>, a prototypical septuple atomic layered two-dimensional material. The low energy electron and hole valleys drift far off the K/K' point under uniaxial strains. The direction and strength of valley drift strongly depend on the nature of the charge carrier and uniaxial strain with a more substantial response along the zigzag path. Our findings exhibit the pivotal role of microscopic orbital contribution and symmetry lowering. The changing geometric properties of Bloch states affect the Berry curvatures and circular dichroism. Specifically, Berry curvature dipole is significantly enhanced under the tensile strain along armchair and zigzag directions. Meanwhile, the particle-hole asymmetry arising from nonequivalent electron and hole valley drifts relaxes the selection rules, thus reducing the degree of circular polarization up to  $\sim 0.98$ . Therefore, strain engineering of valley physics in the monolayer MoSi<sub>2</sub>N<sub>4</sub> is of prime importance for valleytronics.

DOI: [10.1103/PhysRevMaterials.7.114003](https://doi.org/10.1103/PhysRevMaterials.7.114003)

### I. INTRODUCTION

Two-dimensional (2D) layered semiconductors are essential in manipulating the valley degrees of freedom for potential valleytronics devices [1,2]. Several intriguing phenomena are experimentally accomplished, such as the valley Hall effect [3–6], valley excitons [7,8], and valley Zeeman and ac Stark effects [9]. MoSi<sub>2</sub>N<sub>4</sub> is a newly discovered 2D material that has attracted significant scientific attention [10,11]. The monolayer MoSi<sub>2</sub>N<sub>4</sub> has a pair of Dirac valleys at corners of the Brillouin zone (BZ) connected by the time-reversal symmetry operation and constitutes a binary index for low energy carriers [12–17]. The breaking of inversion symmetry and high spin-orbit coupling leads to valley contrasting features in the spin splitting, Berry curvatures, and optical circular dichroism [14,18]. Thus valley polarization can be controlled by optical, transport, and magnetic interactions. Theoretical calculations predict the high electron/hole mobility up to 270/1200 cm<sup>2</sup>V<sup>-1</sup>s<sup>-1</sup> for monolayer MoSi<sub>2</sub>N<sub>4</sub>, which is nearly six times larger than that of monolayer MoS<sub>2</sub> predicted [10]. The excellent stability, carrier mobility, suitable band gap, and protection of capped SiN layer from environmental disturbance promise an advantage over MoS<sub>2</sub> in valley transport properties, especially valley filtering, valley Hall effect, and valley coupled spin Hall effect [10,19].

Strain engineering is used successfully to improve the performance of monolayer devices by modifying the band dispersion. Some groundbreaking discoveries related to strains include band gap reduction [20–23], direct to indirect band transition [24], funneling of photogenerated excitons [25], tunnel resistance modulation [26], enhancement in Rashba

splitting [27–30], and coexistence of negative Poisson's ratio and magnetism [31]. The uniaxial strain can also lower the symmetry, inducing the band splitting and modulation of Berry curvature dipole and valley magnetization [32]. The strain superlattices can open the significant energy gap and shift the Dirac points in graphene [33]. Furthermore, several experimental and theoretical investigations predict the direct to indirect band gap transition in MoS<sub>2</sub> under the tensile strain between 2 to 3% [20,34,35]. Most importantly, 2D materials are able to sustain significant reversible elastic strain, i.e., graphene (25%) [36–38] and MoS<sub>2</sub> (11%) [39–41], making strain-dependent effects easily accessible in experiments.

The strain engineering of monolayer MoSi<sub>2</sub>N<sub>4</sub> has been gaining attention recently [14,42–44]. These previous reports are based on the biaxial or uniaxial out-of-plane strain, where the valley extremum remains at the K/K' point, preserving the threefold rotation symmetry [14,42,44]. However, the effect of reduced symmetry of valleys in monolayer MoSi<sub>2</sub>N<sub>4</sub> remains unexplored. Recent theoretical and experimental studies have shown that the nonlinear Hall effect can occur even in time-reversal symmetric systems under reduced symmetry [32,45–47]. Therefore, the mechanical tunability of its valleys and associated properties in monolayer MoSi<sub>2</sub>N<sub>4</sub> under uniaxial deformation potential provides an ideal avenue to prospect.

This study demonstrates strain-induced electron and hole valley drifts and their effects in monolayer MoSi<sub>2</sub>N<sub>4</sub>. We theoretically apply in-plane lattice deformation up to 10% along three crystallographic nonequivalent directions, i.e., armchair (AC), intermediate (IM), and zigzag (ZZ). The energy valley drifts are responsive to the strain directions. For example, drifts are more pronounced for strain along the ZZ direction than the IM and AC directions. Additionally, electron valleys are more sensitive to the deformation when compared to the hole valleys. The group theoretical perspective and microscopic orbital contribution explain the underlying mechanism

<sup>\*</sup>phz198687@physics.iitd.ac.in

<sup>†</sup>saswata@physics.iitd.ac.in

behind the asymmetric nature of valley drifts. Afterward, we provide the effect of asymmetric valley drifts on Berry curvature distribution and optical circular dichroism.

## II. CALCULATION METHODS

Density functional theory [48,49] calculations were performed using the projector augmented wave method as implemented in the Vienna *ab initio* simulation package (VASP) [50,51]. The Perdew-Burke-Ernzerhof (PBE) pseudopotentials were used for exchange-correlation potential [52]. The BZ was sampled using the Monkhorst-Pack method with a spacing of  $0.02 \text{ \AA}^{-1}$  [53]. A vacuum of  $20 \text{ \AA}$  along the  $z$  direction was used to avoid artificial interaction between periodic images. The Wannier representations were obtained by projecting the Bloch states from first principles calculations on Mo-3*d*, N-2*s*, N-2*p*, and Si-3*p* orbitals [54].

The monolayer  $\text{MoSi}_2\text{N}_4$  has the hexagonal lattice structure built by septuple atomic layers in the sequence N-Si-N-Mo-N-Si-N (see Fig. 1). The lattice can be regarded as a 2H-MoN<sub>2</sub> monolayer sandwiched between two silicene-like Si-N monolayers [10]. There are two alternative choices for the unit cell of monolayer  $\text{MoSi}_2\text{N}_4$  having the  $\overline{P6m}2$  space group. As shown in Fig. 1(a), the choices are the  $\overline{P6m}2:h$  (7 atoms hexagonal lattice) and  $\overline{P6m}2:o$  (14 atoms orthorhombic lattice). It is very efficient to perform DFT calculations in the  $\overline{P6m}2:h$  setting. However, the  $\overline{P6m}2:o$  is of great convenience in terms of symmetry perspective for strained lattice along AC or ZZ directions and therefore considered in our study. First, we have mapped the arbitrary  $k$  point ( $k_1, k_2$ ) of hexagonal BZ on the basis of orthorhombic reciprocal vectors. The results are expressed as [see Sec. I of the Supplemental Material (SM) [55] for more details]

$$(k_1, k_2)_h \Rightarrow (k_1, k_1 + 2k_2)_o. \quad (1)$$

The location of  $\Gamma$ , M, and K points are shown in Fig. 1(d) and corresponds to  $(0, 0, 0)$ ,  $(1/2, 1/2, 0)$ , and  $(1/3, 0, 0)$  in orthorhombic BZ, respectively. First, we have fully relaxed the structure using the conjugate gradient algorithm until the force on every atom is smaller than  $1 \text{ meV/\AA}$ . The simulated lattice parameter ( $a_1$ ) was found to be  $2.912 \text{ \AA}$ , which is in good agreement with the previous experimental [10,11] and theoretical studies [12–17].

To simulate the strained lattice of monolayer  $\text{MoSi}_2\text{N}_4$  along  $x$  (ZZ) and  $y$  (AC) directions, we change the corresponding lattice vector to satisfy the relations  $\epsilon_x = \frac{a'_1 - a_1}{a_1}$  and  $\epsilon_y = \frac{a'_2 - a_2}{a_2}$ , where  $a'_1$  ( $a'_2$ ) and  $a''_1$  ( $a''_2$ ) are the lattice constants along  $x$  ( $y$ ) direction without and with strain, respectively [see Fig. 1(a)]. For the application of strain along an arbitrary direction, we rotate the coordinate system such that  $x'$  points along the direction of strain. After that, we apply strain, relax the structure along  $y'$  direction, and then return to the original Cartesian system. Due to the  $C_{3z}$  and  $M_{yz}$  symmetry, only the directions between  $\theta = 0^\circ$  and  $30^\circ$  are of interest, where  $\theta$  is measured counterclockwise with respect to the ZZ direction. Therefore, we have considered  $\theta = 0^\circ$  (ZZ),  $\theta = 15^\circ$  (IM), and  $\theta = 90^\circ$  (equivalent to  $30^\circ$ ) (AC) directions. For the uniaxially strained lattice,  $D_{3h}$  symmetry reduces to  $C_{2h}$ , containing a twofold rotation operation ( $C_{2z}$ ) and mirror

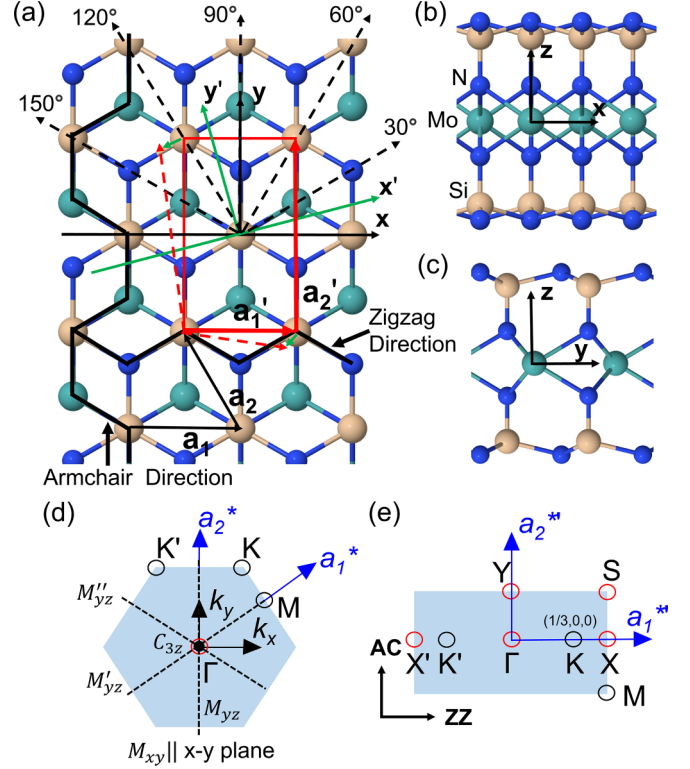


FIG. 1. (a) Top and (b),(c) side views of monolayer  $\text{MoSi}_2\text{N}_4$ . The  $x$ ,  $y$ , and  $z$  axes are shown in each case.  $a_1$  and  $a_2$  are the primitive lattice vectors, while  $a'_1$  and  $a'_2$  are lattice vectors of the orthorhombic cell. The rotated Cartesian frame for strain along an arbitrary direction is shown using green lines. After applying strain along  $x'$  direction and allowing relaxation along perpendicular  $y'$  direction, the orthorhombic unit cell is shown using red dashed lines. The effect of strain on the strained lattice is exaggerated for clear illustration and is much smaller for our considered range.  $x$  and  $y$  directions are zigzag (ZZ) and armchair (AC), respectively. The atomic arrangement is ZZ along  $0^\circ$ ,  $60^\circ$ , and  $120^\circ$ , whereas it is AC along  $30^\circ$ ,  $90^\circ$ , and  $150^\circ$  directions. The first (d) hexagonal and (e) orthorhombic BZ are shown.  $M_{xy}$  and  $M_{yz}$  are the mirror planes and  $C_{3z}$  is the threefold rotation axis. The high symmetry points  $\Gamma$ , M, and K of hexagonal BZ are mapped in the orthorhombic BZ [see Eq. (1)].

symmetry containing the  $x$ - $y$  plane. Moreover, additional diagonal mirror planes arise for the strain along AC and ZZ directions, leading to  $D_{2d}$  point group symmetry.

The elastic energy density for orthorhombic lattices is expressed as [56,57]

$$U_{\text{ortho}} = \frac{1}{2}C_{11}\epsilon_{xx}^2 + \frac{1}{2}C_{22}\epsilon_{yy}^2 + C_{12}\epsilon_{xx}\epsilon_{yy} + C_{44}\epsilon_{xy}^2. \quad (2)$$

$C_{ij}$  and  $\epsilon_{ij}$  are components of elastic constants and strain tensors, respectively. Employing Eq. (2), the direction-dependent Young's modulus and Poisson's ratio are obtained as [56]

$$Y_{2D}(\theta) = \frac{\Delta}{C_{11}s^4 + C_{22}c^4 + \left(\frac{\Delta}{C_{44}-2C_{12}}\right)c^2s^2},$$

$$\nu_{2D}(\theta) = \frac{(C_{11} + C_{22} - \frac{\Delta}{C_{44}})c^2s^2 - C_{12}(s^4 + c^4)}{C_{11}s^4 + C_{22}c^4 + \left(\frac{\Delta}{C_{44}-2C_{12}}\right)c^2s^2}, \quad (3)$$

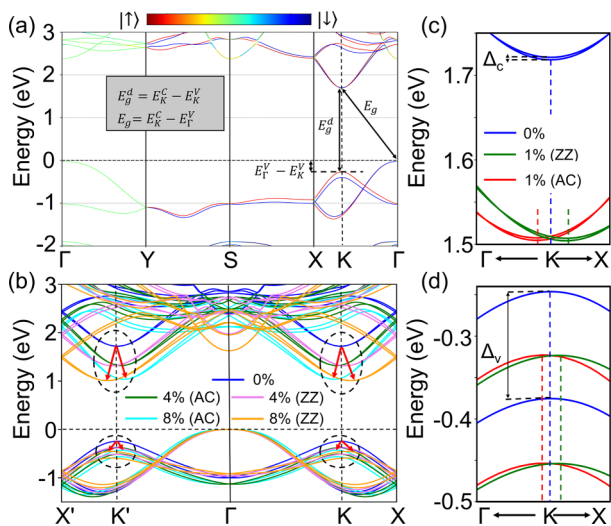


FIG. 2. (a) Spin-projected band structures of the monolayer  $\text{MoSi}_2\text{N}_4$  in the presence of SOC. The red and blue denote the spin-up and spin-down states, respectively. (b) Evolution of band structures under the uniaxial strain of strength 4% and 8% along the ZZ and AC directions. The red arrows represent the valley drifts. Panels (c) and (d) are the zoomed versions of low conduction bands and top valence bands of monolayer  $\text{MoSi}_2\text{N}_4$  with 1% uniaxial strain, respectively. The vertical dashes represent the location of energy extreme in  $k$  space.

where  $\Delta = C_{11}C_{22} - C_{12}^2$ ,  $c = \cos(\theta)$ , and  $s = \sin(\theta)$ . The dynamical and mechanical stabilities of strained lattices are confirmed using phonon spectrum and elastic constants, respectively (see Sec. II of the SM [55]).

### III. RESULTS

Spin-projected band structure of monolayer  $\text{MoSi}_2\text{N}_4$  is shown in Fig. 2. It has a band gap of 1.72 eV, having valence band maximum (VBM) and conduction band minimum (CBM) at the  $\Gamma$  and K points, respectively. The calculated band gap is smaller than the experimental value of 1.94 eV [10] due to self-interaction error, while it is in good agreement with previous theoretical PBE results [12–15]. In Refs. [19,42,58], band gaps are improved using hybrid HSE06 and many-body perturbation theories (GW, BSE). We have conducted a comparison between the results using the PBE and HSE06 to validate the choice of functional (see Sec. III of the SM [55]). The results calculated using HSE06 are within  $\pm 4\%$  as compared to the PBE, excluding band gaps. Therefore, our calculations are based on the computationally efficient PBE functional. The valence band (VB) at K points lies lower in energy than VBM with an offset ( $\Delta_{\Gamma-K} = E_{\Gamma}^V - E_K^V$ ) value of 0.24 eV [see Fig. 2(a)]. Spins' eigenstates are polarized along the  $z$  direction except for the  $\Gamma$ -Y line and can be explained by the symmetry aspects [15]. Horizontal-mirror symmetry ( $M_{xy}$ ) commutes with the Hamiltonian, therefore eliminating the spin polarization along the  $x$ - $y$  plane and preserving it along the  $z$  direction. For any  $k$  point along the  $\Gamma$ -Y direction,  $H(k)$  exhibits  $C_{2v}$  point group symmetry and does not contain the spin operator leading to degenerate eigenvalues. It has Dirac-type valley bands near the K/K'

points. Due to the strong SOC and broken inversion symmetry, valley fermions exhibit strong spin-valley coupling, valley-selective optical circular polarization, and valley-contrasting Berry curvature [13–15]. The VB valley is the spin split of order  $\sim 130$  meV, whereas the CB valley is nearly spin degenerate (see Sec. IV of the SM [55]). These effects are well explained by the previous DFT calculations [13–15,59], tight-binding (TB) models [15], and two-band and three-band  $k \cdot p$  models [13,14].

Figure 2(b) shows the evolution of band structures under the strain along AC and ZZ directions. We find a robust strain-valley coupling between the strain and low-energy states. Uniaxial strain shifts the electron and hole valleys away from the K/K' point. Figures 2(c) and 2(d) show the valley drift response of low CB and top VB under the uniaxial strain in the limit of 1% along ZZ and AC directions. Here, we observe that electron valley responses are stronger when compared to the hole sector. In addition, the parabolicity of bands is more heavily deformed than the hole bands. This phenomenon can be explained by the changing geometric effects and orbital hybridization of relevant Bloch states due to reduced symmetry of the lattice. The strain modifies the scalar potential for the corresponding Bloch bands contributing to the low-energy holes and valley states at the K/K' point.

For a clear illustration of valley drifts, we have plotted the constant energy contours of VB and CB near the K point. The results are shown in Figs. 3(a) and 3(b) (see Sec. V of the SM [55] for energy contours in the entire BZ). Except for the immediate vicinity of the K point, the dispersion is not isotropic. The trigonal warping effect of energy bands is visible, resulting from the  $C_{3z}$ . The trigonal warping effect is more pronounced for the VB when compared to the CB. When applying the uniaxial strain, an increase in the warping effect near the K point is observed due to the continuous reduction in  $C_{3z}$  and translation symmetry along its mutually perpendicular direction. The bands are elliptically warped (due to the appearance of twofold rotation symmetry) in the immediate proximity of K when uniaxial strain is applied and increases with an increasing strain field. The elliptical warping of band topology is antisymmetric in such a way that the major axis is along the  $k_x$  and  $k_y$  direction for strain along ZZ and AC directions, respectively. For lattice strained along the IM direction, the major axis of elliptical warping makes an angle of  $30^\circ$ . The anisotropic nature of electronic bands leads to different effective masses, charge transport, and optical absorption in different directions. In addition, the energy extreme of the valley drifts away from the K point. In general, the direction of valley drift is  $2\theta$  (with respect to the  $K \rightarrow X$  direction) when strain is applied along the  $\theta$  direction. Particularly, the direction of valley drift is  $K \rightarrow \Gamma$  and  $K \rightarrow X$  for AC and ZZ directions, respectively [shown by black arrows in Figs. 3(a) and 3(b)]. To quantify the valley drifts, we plot the valley extreme as a function of strain in Fig. 3(c). The VB drift off the K point with the rate  $1.38 \times 10^{-3} (\frac{2\pi}{a})/\%$  for strain along the AC direction, whereas the rate of drift is  $2.19 \times 10^{-3} (\frac{2\pi}{a})/\%$  for the ZZ direction. For uniaxial strain along the IM direction, drift is between that of the AC or ZZ direction with the rate of  $1.99 \times 10^{-3} (\frac{2\pi}{a})/\%$ . Similarly, the rates of electron valley drifts are  $2.17 \times 10^{-3} (\frac{2\pi}{a})/\%$ ,  $3.43 \times 10^{-3} (\frac{2\pi}{a})/\%$ , and  $3.89 \times 10^{-3} (\frac{2\pi}{a})/\%$  for strain along

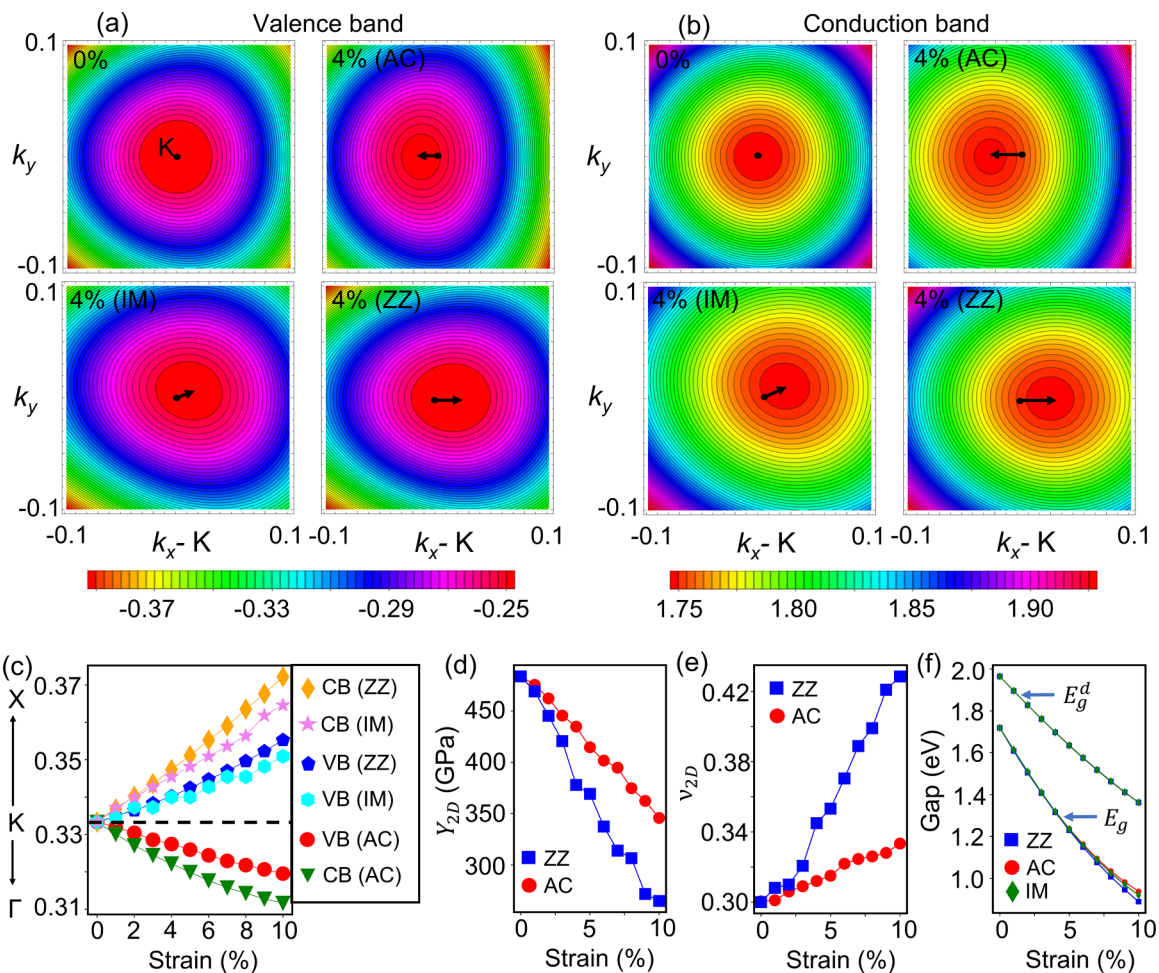


FIG. 3. (a) Contour plot showing isoenergy contours of the valence band around the K point for the unstrained case (0%) and with the uniaxial strain of 4% along AC, IM, and ZZ directions of monolayer  $\text{MoSi}_2\text{N}_4$ . Black arrows show the directions of valley drifts. (b) The same as in (a) for the conduction band. (c) Momentum drift of the CB and VB near the K point. Valley extremum as a function of uniaxial strain applied along the AC, IM, and ZZ directions. Note that only the  $k_x$  component of drift along  $\text{K} \rightarrow \text{X}$ ,  $\cos(30^\circ)$  of the net drift, is shown in (c) for the IM case. The  $k_y$  component [ $\sin(30^\circ)$  of the net drift] is also there and duly considered in all the calculations. The variation of (d) Young's modulus, (e) Poisson ratio, and (f) direct and indirect band gap as a function of strain.

the AC, IM, and ZZ directions, respectively. The electron valley drifts are nearly  $\sim 1.7$  times that of hole valley drifts.

Here, we notice that the drift response is more extensive when the lattice is stretched along the ZZ direction. That is because the stretching of the Mo-N bond is asymmetric when the lattice is stretched along the AC or ZZ direction [see Figs. 1(b) and 1(c)]. To understand this, we plot Young's modulus [ $Y_{2D}(\theta)$ ] and Poisson's ratio [ $\nu_{2D}(\theta)$ ] as a function of strain in Figs. 3(d) and 3(e). For unstrained monolayer  $\text{MoSi}_2\text{N}_4$ , Young's modulus 485.7 GPa is in good agreement with the experiment value of  $491.4 \pm 139.1$  GPa [10] and theoretical value of 479 GPa [43]. The drop in Young's modulus is significant when strain is along the ZZ direction. Drastic variation in elastic constants leads to significant cell deformation. Therefore, electron and hole valley drifts are more pronounced when uniaxial strain is applied along the ZZ direction.

Figure 3(f) shows the evolution of direct ( $E_g^d$ ) and indirect ( $E_g$ ) band gaps. The band gap energies are redshifted under the uniaxial tensile strain. The shift in the band gap is nearly direction independent for the smaller strains in the range of

0–5%. However, band gaps are redshifted at a faster rate for the larger uniaxial strains along the ZZ directions and are attributed to the more enormous variation in mechanical constants. The redshift rates of the indirect and direct band gaps are 0.067 eV/% and 0.53 eV/%, respectively. These unequal rates lead to the enhancement in the valence band energy offset ( $\Delta_{\Gamma-K}$ ).  $\Delta_{\Gamma-K}$  increases from 0.24 to 0.43 eV under the uniaxial strain of 10%. The optical absorption and photoluminescence experiments study these variations in the band gaps and are widely explored for graphene [33,60,61] and TMDs [20,62].

The degeneracy of each level is determined by the irreducible representations of point group symmetry of the monolayer that is contained in the full rotation symmetry group [63]. The representation of a full rotation group will be a reducible representation of the  $D_{3h}$  group and can be written as  $\Gamma_{l=2} = A' \oplus E' \oplus E''$ , where  $A'$ ,  $E'$ , and  $E''$  are the irreducible representations of the  $D_{3h}$  point group. Therefore, the fivefold degenerate Mo- $d$  orbitals split into three categories at the  $\Gamma$  point:  $A'(d_z^2)$ ,  $E'(d_{x^2-y^2}, d_{xy})$ , and  $E''(d_{xz}, d_{yz})$  under the effect of the trigonal crystal field. The group of

TABLE I. Irreducible representations and basis functions for the little group  $C_{3h}(=C_3 \times \sigma_h)$  of K/K' point [63]. The sign  $\pm$  corresponds to  $\pm K$  points. The last column contains the energy bands to which basis functions contribute.

$C_{3h}$	$C_3$	$\sigma_h$	Mo	N	Band
$A'$	1	1	$ \Psi_{2,\mp 2}^{\text{Mo}}\rangle$	$\frac{1}{\sqrt{2}}( \Psi_{1,\mp 1}^{\text{N1}}\rangle +  \Psi_{1,\mp 1}^{\text{N2}}\rangle)$	VB
$A''$	1	-1	$ \Psi_{2,\pm 1}^{\text{Mo}}\rangle$	$\frac{1}{\sqrt{2}}( \Psi_{1,\mp 1}^{\text{N1}}\rangle -  \Psi_{1,\mp 1}^{\text{N2}}\rangle)$	CB + 1
$E'_1$	$\omega^\pm$	1	$ \Psi_{2,0}^{\text{Mo}}\rangle$	$\frac{1}{\sqrt{2}}( \Psi_{1,\pm 1}^{\text{N1}}\rangle +  \Psi_{1,\pm 1}^{\text{N2}}\rangle)$	CB
$E'_2$	$\omega^\mp$	1	$ \Psi_{2,\pm 2}^{\text{Mo}}\rangle$	$\frac{1}{\sqrt{2}}( \Psi_{1,0}^{\text{N1}}\rangle -  \Psi_{1,0}^{\text{N2}}\rangle)$	CB + 2
$E''_1$	$\omega^\pm$	-1	$ \Psi_{1,0}^{\text{Mo}}\rangle$	$\frac{1}{\sqrt{2}}( \Psi_{1,\pm 1}^{\text{N1}}\rangle -  \Psi_{1,\pm 1}^{\text{N2}}\rangle)$	VB - 2
$E''_2$	$\omega^\mp$	-1	$ \Psi_{2,\mp 1}^{\text{Mo}}\rangle$	$\frac{1}{\sqrt{2}}( \Psi_{1,0}^{\text{N1}}\rangle +  \Psi_{1,0}^{\text{N2}}\rangle)$	VB - 1

wave vector at the K/K' point reduces to the  $C_{3h}$ . Further, we constructed the Bloch state using the linear combination of atomic orbitals approach,  $\Psi_{l,m}^\eta(r, k) = \sum_{R_\eta} e^{ik \cdot R_\eta} Y_l^m(r - R_\eta)$ , where  $Y_l^m$  are the spherical harmonics and  $R_\eta$  is the position of Mo, N, and Si atoms. We then identify how the Bloch wave function  $\Psi_{l,m}^\eta(r, k)$  transforms under the symmetry operations of  $C_{3h}$ . Table I classifies the Bloch state at the BZ corners according to the irreducible representations of  $C_{3h}$ . The  $M_{xy}$  mirror symmetry allows hybridization only between  $A'$  and  $E'$  orbitals, opening a gap at the K point [6]. As seen from Figs. 4(a) and 4(b), the VB and CB states mainly originate from the hybridization of Mo- $d$  and N- $p$  orbitals. The Bloch state contributing to CB at the K/K' point is  $|\Psi_{2,0}^{\text{Mo}}\rangle$ , whereas the states for VB are  $|\Psi_{2,-2}^{\text{Mo}}\rangle$  and  $|\Psi_{2,2}^{\text{Mo}}\rangle$  at the K and K', respectively. The periodic parts of the Bloch wave functions for the CB and VB at the K point are predominantly composed of  $|d_{z^2}\rangle$  and  $|d_{x^2-y^2}-id_{xy}\rangle$ , respectively. The uniaxial strain modifies the crystal field between metal and the Mo-N

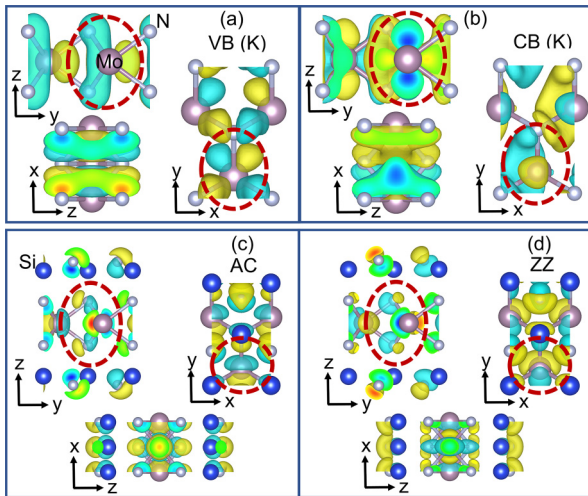


FIG. 4. Real part of the wave function of (a) VB and (b) CB at the K point for monolayer  $\text{MoSi}_2\text{N}_4$  without strain. Note that, in (a) and (b), we show only the Mo-N<sub>2</sub> network since the contribution coming from the upper and lower Si-N layer is almost zero. The charge density difference between the unstrained and 4% strained lattice along the (c) AC and (d) ZZ directions. The electron accumulation is shown in cyan and electron depletion is shown in yellow.

trigonal coordination environment. Therefore, strain modifies the bandwidths of contributing orbitals and energy of the Bloch states. The energy of  $d$  and  $p$  orbitals along the strain direction increases with increasing strain. The out-of-plane orbitals ( $d_{z^2}$ ) are more influenced by the in-plane strain when compared to the in-plane orbital ( $d_{x^2-y^2}, d_{xy}$ ). Therefore, the effect of strain is more prominent for electron valleys leading to larger valley drift for CB. Stretching of orbitals along the strain direction leads to the charge density redistribution and increases with the increasing strain field. To compare the ZZ and AC directions, we plot the ground state charge density difference between the unstrained lattice and the lattice with 4% of strain. The charge density difference near Mo and inner N atoms is more prominent in the ZZ case compared to the AC case. Strong charge density redistribution leads to sharper changes in the valley drifts, elastic constants, and band gaps for the lattice stretched along the ZZ direction.

We further investigate the Berry curvatures in monolayer  $\text{MoSi}_2\text{N}_4$  under uniaxial strain. Berry curvature is analogous to the magnetic field in momentum space and has a pivotal impact on the electronic transport properties. For example, the integral of Berry curvature gives Hall conductivity. The Berry curvature is evaluated using the expression

$$\Omega(k) = i\nabla_k \times \langle u(k) | \nabla_k | u(k) \rangle, \quad (4)$$

where  $|u(k)\rangle$  is the periodic part of the Bloch wave function. We plot the total Berry curvature of all the occupied bands in Fig. 5(a). Berry curvature distribution is peaked around valleys with opposite values at K and K' points. The contrasting nature of Berry curvatures at the valleys is attributed to the time-reversal symmetry, enabling the separation of charge carriers depending on their valley index. The introduction of strain alters the occupation of different orbitals contributing to Bloch states and leading to modification in the electronic energies and Berry curvature. The Berry curvature profile is strongly modified when the lattice is strained along the ZZ or AC direction. The Berry curvature peak drifts away from the K/K' point, similar to the energy valley drift. The Berry curvature peak is enhanced up to a factor of  $\sim 1.5$  under the strain of 8% along ZZ and AC directions. The increased Berry curvature flux density and drift would influence the valley transport when the external transverse electric field is applied since the Berry curvature directly enters into the equation of motion and engenders an anomalous velocity term  $\sim E \times \Omega$ . Therein, the strong response of valleys to the strain notably alters the valley-contrasting physics in the monolayer  $\text{MoSi}_2\text{N}_4$ .

The electron and hole population in two nonequivalent valleys are controlled by circularly polarized optical pumping. The electromagnetic interaction that gives rise to dipole transition is  $H_{em} = \frac{e}{mc} P \cdot A$ , where  $P$  is the momentum operator and  $A$  is the magnetic vector potential of incident light [63]. Then, the probability of dipole transition between the VB  $|v(k)\rangle$  and CB  $|c(k)\rangle$  is  $|\langle v(k) | H_{em} | c(k) \rangle|^2$ . Group theory tells when the dipole transition is allowed or forbidden [63]. The wave functions  $v(k)$  and  $c(k)$  at the K point transform as the irreducible representations  $A'$  and  $E'_1$ , respectively (see Table I).  $P_\pm (= P_x \pm iP_y)$  are the chiral momentum operators representing right/left-hand circularly polarized light.  $P_\pm (= P_x \pm iP_y)$  transforms as  $C_3 P_\pm C_3^\dagger = \omega^\mp P_\pm$  [13].  $P_+$  transforms according to the irreducible representation  $E'_2$ .

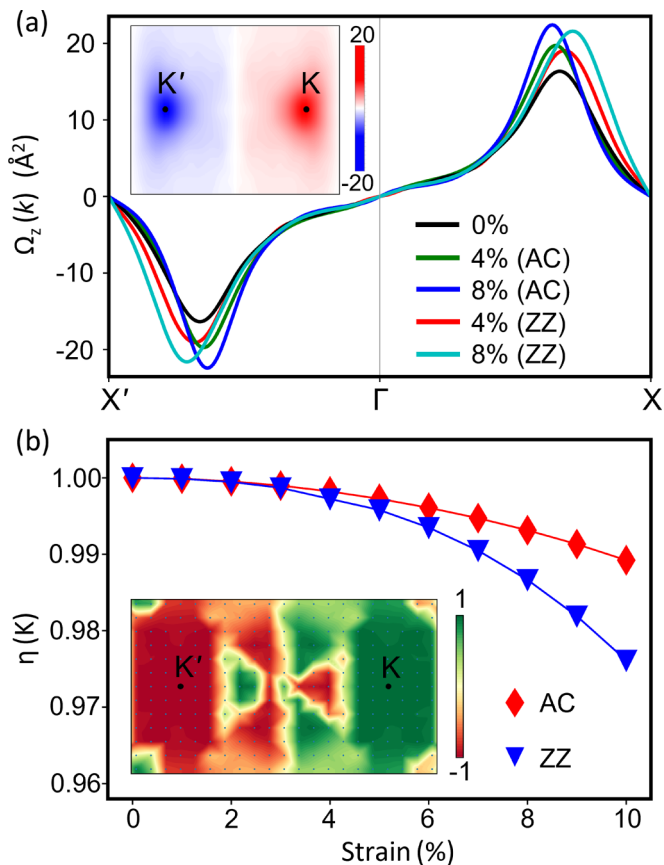


FIG. 5. (a) Berry curvature distribution summed for all valence bands along the path  $X'-K'-\Gamma-K-X$  in monolayer  $\text{MoSi}_2\text{N}_4$ . Inset in (a) shows the mapping of Berry curvature under the first BZ. (b) The degree of circular polarization of excitation from VB to CB at the K point. Inset in (b) shows the mapping of the degree of circular polarization in the first BZ.

$A' \otimes E_2' \otimes E_1'$  contains only the fully symmetrical irreducible representation  $A'$ . Therefore, right-hand circularly polarized light will be absorbed at the K point, whereas absorbance of left-hand circularly polarized light will be forbidden. A similar analysis shows that only left-hand circularly polarized light will be absorbed at the time-reversal conjugate  $K'$  point. The degrees of circular polarization  $[\eta(k)]$  are expressed as

$$\eta(k) = \frac{|P_+|^2 - |P_-|^2}{|P_+|^2 + |P_-|^2}. \quad (5)$$

We calculate the degree of circular polarization using the DFT and the results agree with the symmetry analysis [see inset in Fig. 5(b)]. The transition is exclusively coupled to a specific circular polarization at the valley center for zero strain. After introducing strain, the  $\eta(k)$  at the K point decreases due to the continuous reduction of the group of wave vectors from  $C_{3h}$  to  $C_{2h}$ . The unequal rates of electron and hole valley drifts soften the valley-selective optical selection rules arising from the  $C_3$  symmetry operation due to changes in its optical matrix elements  $[\langle v(k)|P_{\pm}|c(k)\rangle]$ . The  $\eta(k)$  reduces up to 0.99 and 0.98 for 10% uniaxially strained  $\text{MoSi}_2\text{N}_4$  along AC and ZZ directions, respectively [see Fig. 5(b)]. Therefore, uniaxial

strain makes monolayer  $\text{MoSi}_2\text{N}_4$  less valley selective and effects are more prominent along the ZZ direction.

Finally, we emphasize that the analysis presented here can also be manifested in other septuple-layered  $\text{MA}_2\text{Z}_4$  ( $M = \text{Cr}, \text{Mo}, \text{W}, \text{V}$ ;  $A = \text{Si}, \text{Ge}$ ;  $Z = \text{N}, \text{P}, \text{As}$ ) materials [10]. However, the strength of effects can be different. In addition, there are no states other than K/ $K'$  near the Fermi level in monolayers  $\text{MA}_2\text{P}_4$  and  $\text{MA}_2\text{As}_4$  [12,17]. Therefore, interference from the different parts of BZ will be minimal, providing an additional advantage over the monolayer  $\text{MoSi}_2\text{N}_4$ . Furthermore, geometric properties of Bloch states other than Berry curvature can also be modified with the uniaxial strain. For example, orbital magnetic moments ( $m_{nk}$ ) are normal to the plane for 2D materials and have opposite nature for the K and  $K'$  valleys. Orbital moments tuning allows control over valley polarization by a vertical magnetic field [64].

#### IV. SUMMARY AND OUTLOOK

We have reported valley drifts in uniaxially strained monolayer  $\text{MoSi}_2\text{N}_4$ . By taking strain along AC, IM, and ZZ directions, we confirmed the stronger strain-valley coupling along the ZZ direction due to pronounced geometric deformation. Additionally, electron valleys show a faster response (nearly 1.7 times) to the strain than hole valleys owing to contribution coming from out-of-plane  $d_{z^2}$  orbitals. The observed rates of valley drifts are up to  $3.89 \times 10^{-3}(\frac{2\pi}{a})/\%$ . These effects noticeably affect the valley's selective optical excitation. The reduction of threefold rotation symmetry leads to a substantial drop in the degree of circular polarization to  $\sim 0.98$ . Besides, valley drifts influence the Berry curvature profile around the K/ $K'$  point, where an increase in the flux along with drift can induce the valley current in monolayer  $\text{MoSi}_2\text{N}_4$ . This strong valley asymmetry between valley carriers directly results from changing geometric and orbital effects under directional lattice strain that reduces the lattice symmetry.

Valley drifts lead to the pure electrical generation of valley magnetization in 2D materials through magnetoelectric effect and its direct imaging by Kerr rotation microscopy [47]. The strength and direction of uniaxial strain can be controlled using stretchable van der Waals heterostructures [32]. The valley drift observed in monolayer  $\text{MoSi}_2\text{N}_4$  is larger than graphene  $[\sim 0.6 \times 10^{-3}(\frac{2\pi}{a})/\%]$  [65] and similar to monolayer  $\text{MoS}_2$   $[\sim 4.5 \times 10^{-3}(\frac{2\pi}{a})/\%]$  [35,66]. In addition, high-carrier mobility ( $\sim 2.29 \times 10^3 \text{ cm}^2\text{V}^{-1}\text{s}^{-1}$  [67]) and excellent ambient stability [10] make strained monolayer  $\text{MoSi}_2\text{N}_4$  a suitable candidate to observe the Berry curvature dipole induced nonlinear Hall effect [45,46]. Moreover, the drop in degree of circular polarization in monolayer  $\text{MoSi}_2\text{N}_4$  is smaller than monolayer  $\text{MoS}_2$  ( $\sim 0.95$  [68]) under similar strain, making valley polarization by optical pumping more robust to the strain. Our theoretical finding in this work may trigger valley-based electronic and optoelectronic applications in  $\text{MoSi}_2\text{N}_4$  monolayers under in-plane lattice strain.

#### ACKNOWLEDGMENTS

S.S. acknowledges CSIR, India, for the senior research fellowship [Grant No. 09/086(1432)/2019-EMR-I]. S.B.

acknowledges financial support from SERB under a core research grant (Grant No. CRG/2019/000647) to set up his

High-Performance Computing (HPC) facility “Veena” at IIT Delhi for computational resources.

- [1] J. R. Schaibley, H. Yu, G. Clark, P. Rivera, J. S. Ross, K. L. Seyler, W. Yao, and X. Xu, Valleytronics in 2D materials, *Nat. Rev. Mater.* **1**, 16055 (2016).
- [2] S. A. Vitale, D. Nezhich, J. O. Varghese, P. Kim, N. Gedik, P. Jarillo-Herrero, D. Xiao, and M. Rothschild, Valleytronics: Opportunities, challenges, and paths forward, *Small* **14**, 1801483 (2018).
- [3] R. V. Gorbachev, J. C. W. Song, G. L. Yu, A. V. Kretinin, F. Withers, Y. Cao, A. Mishchenko, I. V. Grigorieva, K. S. Novoselov, L. S. Levitov, and A. K. Geim, Detecting topological currents in graphene superlattices, *Science* **346**, 448 (2014).
- [4] K. F. Mak, K. L. McGill, J. Park, and P. L. McEuen, The valley Hall effect in MoS<sub>2</sub> transistors, *Science* **344**, 1489 (2014).
- [5] J. Lee, K. F. Mak, and J. Shan, Electrical control of the valley Hall effect in bilayer MoS<sub>2</sub> transistors, *Nat. Nanotechnol.* **11**, 421 (2016).
- [6] D. Xiao, G.-B. Liu, W. Feng, X. Xu, and W. Yao, Coupled spin and valley physics in monolayers of MoS<sub>2</sub> and other group-vi dichalcogenides, *Phys. Rev. Lett.* **108**, 196802 (2012).
- [7] A. Chernikov, T. C. Berkelbach, H. M. Hill, A. Rigosi, Y. Li, B. Aslan, D. R. Reichman, M. S. Hybertsen, and T. F. Heinz, Exciton binding energy and nonhydrogenic Rydberg series in monolayer WS<sub>2</sub>, *Phys. Rev. Lett.* **113**, 076802 (2014).
- [8] Z. Ye, T. Cao, K. O’Brien, H. Zhu, X. Yin, Y. Wang, S. G. Louie, and X. Zhang, Probing excitonic dark states in single-layer tungsten disulphide, *Nature (London)* **513**, 214 (2014).
- [9] H. Rostami and R. Asgari, Valley Zeeman effect and spin-valley polarized conductance in monolayer MoS<sub>2</sub> in a perpendicular magnetic field, *Phys. Rev. B* **91**, 075433 (2015).
- [10] Y.-L. Hong, Z. Liu, L. Wang, T. Zhou, W. Ma, C. Xu, S. Feng, L. Chen, M.-L. Chen, D.-M. Sun, X.-Q. Chen, H.-M. Cheng, and W. Ren, Chemical vapor deposition of layered two-dimensional MoSi<sub>2</sub>N<sub>4</sub> materials, *Science* **369**, 670 (2020).
- [11] Z. Liu, L. Wang, Y.-L. Hong, X.-Q. Chen, H.-M. Cheng, and W. Ren, Two-dimensional superconducting MoSi<sub>2</sub>N<sub>4</sub>(MoN)<sub>4n</sub> homologous compounds, *Natl. Sci. Rev.* **10**, nwac273 (2022).
- [12] L. Wang, Y. Shi, M. Liu, A. Zhang, Y.-L. Hong, R. Li, Q. Gao, M. Chen, W. Ren, H.-M. Cheng, Y. Li, and X.-Q. Chen, Intercalated architecture of MA<sub>2</sub>Z<sub>4</sub> family layered van der Waals materials with emerging topological, magnetic and superconducting properties, *Nat. Commun.* **12**, 2361 (2021).
- [13] C. Yang, Z. Song, X. Sun, and J. Lu, Valley pseudospin in monolayer MoSi<sub>2</sub>N<sub>4</sub> and MoSi<sub>2</sub>As<sub>4</sub>, *Phys. Rev. B* **103**, 035308 (2021).
- [14] S. Li, W. Wu, X. Feng, S. Guan, W. Feng, Y. Yao, and S. A. Yang, Valley-dependent properties of monolayer MoSi<sub>2</sub>N<sub>4</sub>, WSi<sub>2</sub>N<sub>4</sub>, and MoSi<sub>2</sub>As<sub>4</sub>, *Phys. Rev. B* **102**, 235435 (2020).
- [15] Z. Wang, X. Kuang, G. Yu, P. Zhao, H. Zhong, and S. Yuan, Electronic properties and quasiparticle model of monolayer MoSi<sub>2</sub>N<sub>4</sub>, *Phys. Rev. B* **104**, 155110 (2021).
- [16] R. Islam, B. Ghosh, C. Autieri, S. Chowdhury, A. Bansil, A. Agarwal, and B. Singh, Tunable spin polarization and electronic structure of bottom-up synthesized MoSi<sub>2</sub>N<sub>4</sub> materials, *Phys. Rev. B* **104**, L201112 (2021).
- [17] H. Ai, D. Liu, J. Geng, S. Wang, K. H. Lo, and H. Pan, Theoretical evidence of the spin–valley coupling and valley polarization in two-dimensional MoSi<sub>2</sub>X<sub>4</sub>(X= N, P, and As), *Phys. Chem. Chem. Phys.* **23**, 3144 (2021).
- [18] S. Sheoran, S. Monga, A. Phutela, and S. Bhattacharya, Coupled spin-valley, rashba effect, and hidden spin polarization in WSi<sub>2</sub>N<sub>4</sub> family, *J. Phys. Chem. Lett.* **14**, 1494 (2023).
- [19] Y. Wu, Z. Tang, W. Xia, W. Gao, F. Jia, Y. Zhang, W. Zhu, W. Zhang, and P. Zhang, Prediction of protected band edge states and dielectric tunable quasiparticle and excitonic properties of monolayer MoSi<sub>2</sub>N<sub>4</sub>, *npj Comput. Mater.* **8**, 129 (2022).
- [20] C. R. Zhu, G. Wang, B. L. Liu, X. Marie, X. F. Qiao, X. Zhang, X. X. Wu, H. Fan, P. H. Tan, T. Amand, and B. Urbaszek, Strain tuning of optical emission energy and polarization in monolayer and bilayer MoS<sub>2</sub>, *Phys. Rev. B* **88**, 121301(R) (2013).
- [21] A. Castellanos-Gomez, R. Roldán, E. Cappelluti, M. Buscema, F. Guinea, H. S. van der Zant, and G. A. Steele, Local strain engineering in atomically thin MoS<sub>2</sub>, *Nano Lett.* **13**, 5361 (2013).
- [22] H. Rostami, R. Roldán, E. Cappelluti, R. Asgari, and F. Guinea, Theory of strain in single-layer transition metal dichalcogenides, *Phys. Rev. B* **92**, 195402 (2015).
- [23] H. Rostami, R. Asgari, and F. Guinea, Edge modes in zigzag and armchair ribbons of monolayer MoS<sub>2</sub>, *J. Phys.: Condens. Matter* **28**, 495001 (2016).
- [24] H. J. Conley, B. Wang, J. I. Ziegler, R. F. Haglund, Jr., S. T. Pantelides, and K. I. Bolotin, Bandgap engineering of strained monolayer and bilayer MoS<sub>2</sub>, *Nano Lett.* **13**, 3626 (2013).
- [25] P. San-Jose, V. Parente, F. Guinea, R. Roldán, and E. Prada, Inverse funnel effect of excitons in strained black phosphorus, *Phys. Rev. X* **6**, 031046 (2016).
- [26] D. Fu, J. Zhou, S. Tongay, K. Liu, W. Fan, T.-J. King Liu, and J. Wu, Mechanically modulated tunneling resistance in monolayer MoS<sub>2</sub>, *Appl. Phys. Lett.* **103**, 183105 (2013).
- [27] P. Gentile, M. Cuoco, and C. Ortix, Edge states and topological insulating phases generated by curving a nanowire with rashba spin-orbit coupling, *Phys. Rev. Lett.* **115**, 256801 (2015).
- [28] S. Sheoran, P. Bhumla, and S. Bhattacharya, Emergence of cubic ordered full-plane persistent spin textures in lead-free materials, *Phys. Rev. Mater.* **6**, 094602 (2022).
- [29] S. Sheoran, M. Kumar, P. Bhumla, and S. Bhattacharya, Rashba spin splitting and anomalous spin textures in the bulk ferroelectric oxide perovskite KIO<sub>3</sub>, *Mater. Adv.* **3**, 4170 (2022).
- [30] P. Bhumla, D. Gill, S. Sheoran, and S. Bhattacharya, Origin of rashba spin splitting and strain tunability in ferroelectric bulk CsPbF<sub>3</sub>, *J. Phys. Chem. Lett.* **12**, 9539 (2021).
- [31] M.-H. Zhu, X.-J. Weng, G. Gao, S. Dong, L.-F. Lin, W.-H. Wang, Q. Zhu, A. R. Oganov, X. Dong, Y. Tian, X.-F. Zhou, and H.-T. Wang, Magnetic borophenes from an evolutionary search, *Phys. Rev. B* **99**, 205412 (2019).
- [32] J. Son, K.-H. Kim, Y. H. Ahn, H.-W. Lee, and J. Lee, Strain engineering of the Berry curvature dipole and valley magnetization in monolayer MoS<sub>2</sub>, *Phys. Rev. Lett.* **123**, 036806 (2019).

- [33] F. Guinea, M. Katsnelson, and A. Geim, Energy gaps and a zero-field quantum Hall effect in graphene by strain engineering, *Nat. Phys.* **6**, 30 (2010).
- [34] B. G. Shin, G. H. Han, S. J. Yun, H. M. Oh, J. J. Bae, Y. J. Song, C.-Y. Park, and Y. H. Lee, Indirect bandgap puddles in monolayer MoS<sub>2</sub> by substrate-induced local strain, *Adv. Mater.* **28**, 9378 (2016).
- [35] N. Jena, Dimple, R. Ahammed, A. Rawat, M. K. Mohanta, and A. De Sarkar, Valley drift and valley current modulation in strained monolayer MoS<sub>2</sub>, *Phys. Rev. B* **100**, 165413 (2019).
- [36] C. Lee, X. Wei, J. W. Kysar, and J. Hone, Measurement of the elastic properties and intrinsic strength of monolayer graphene, *Science* **321**, 385 (2008).
- [37] K. S. Kim, Y. Zhao, H. Jang, S. Y. Lee, J. M. Kim, K. S. Kim, J.-H. Ahn, P. Kim, J.-Y. Choi, and B. H. Hong, Large-scale pattern growth of graphene films for stretchable transparent electrodes, *Nature (London)* **457**, 706 (2009).
- [38] K. Cao, S. Feng, Y. Han, L. Gao, T. Hue Ly, Z. Xu, and Y. Lu, Elastic straining of free-standing monolayer graphene, *Nat. Commun.* **11**, 284 (2020).
- [39] S. Bertolazzi, J. Brivio, and A. Kis, Stretching and breaking of ultrathin MoS<sub>2</sub>, *ACS Nano* **5**, 9703 (2011).
- [40] K. Liu, X. Chen, P. Gong, R. Yu, J. Wu, L. Li, W. Han, S. Yang, C. Zhang, J. Deng, A. Li, Q. Zhang, F. Zhuge, and T. Zhai, Approaching strain limit of two-dimensional MoS<sub>2</sub> via chalcogenide substitution, *Sci. Bull.* **67**, 45 (2022).
- [41] K. He, C. Poole, K. F. Mak, and J. Shan, Experimental demonstration of continuous electronic structure tuning via strain in atomically thin MoS<sub>2</sub>, *Nano Lett.* **13**, 2931 (2013).
- [42] D. Liang, S. Xu, P. Lu, and Y. Cai, Highly tunable and strongly bound exciton in MoSi<sub>2</sub>N<sub>4</sub> via strain engineering, *Phys. Rev. B* **105**, 195302 (2022).
- [43] B. Mortazavi, B. Javvaji, F. Shojaei, T. Rabczuk, A. V. Shapeev, and X. Zhuang, Exceptional piezoelectricity, high thermal conductivity and stiffness and promising photocatalysis in two-dimensional MoSi<sub>2</sub>N<sub>4</sub> family confirmed by first-principles, *Nano Energy* **82**, 105716 (2021).
- [44] L. Kang and Z. Lin, Second harmonic generation of MoSi<sub>2</sub>N<sub>4</sub>-type layers, *Phys. Rev. B* **103**, 195404 (2021).
- [45] I. Sodemann and L. Fu, Quantum nonlinear hall effect induced by Berry curvature dipole in time-reversal invariant materials, *Phys. Rev. Lett.* **115**, 216806 (2015).
- [46] T. Low, Y. Jiang, and F. Guinea, Topological currents in black phosphorus with broken inversion symmetry, *Phys. Rev. B* **92**, 235447 (2015).
- [47] J. Lee, Z. Wang, H. Xie, K. F. Mak, and J. Shan, Valley magnetoelectricity in single-layer MoS<sub>2</sub>, *Nat. Mater.* **16**, 887 (2017).
- [48] P. Hohenberg and W. Kohn, Inhomogeneous electron gas, *Phys. Rev.* **136**, B864 (1964).
- [49] W. Kohn and L. J. Sham, Self-consistent equations including exchange and correlation effects, *Phys. Rev.* **140**, A1133 (1965).
- [50] G. Kresse and J. Furthmüller, Efficiency of *ab-initio* total energy calculations for metals and semiconductors using a plane-wave basis set, *Comput. Mater. Sci.* **6**, 15 (1996).
- [51] G. Kresse and J. Furthmüller, Efficient iterative schemes for *ab initio* total-energy calculations using a plane-wave basis set, *Phys. Rev. B* **54**, 11169 (1996).
- [52] J. P. Perdew, K. Burke, and M. Ernzerhof, Generalized gradient approximation made simple, *Phys. Rev. Lett.* **77**, 3865 (1996).
- [53] H. J. Monkhorst and J. D. Pack, Special points for Brillouin-zone integrations, *Phys. Rev. B* **13**, 5188 (1976).
- [54] A. A. Mostofi, J. R. Yates, Y.-S. Lee, I. Souza, D. Vanderbilt, and N. Marzari, wannier90: A tool for obtaining maximally-localised wannier functions, *Comput. Phys. Commun.* **178**, 685 (2008).
- [55] See Supplemental Material at <http://link.aps.org/supplemental/10.1103/PhysRevMaterials.7.114003> for coordinate system, stability analysis, comparison of PBE and HSE06 functional, variation of spin splitting with uniaxial strain, and constant energy contours in the full BZ, which also include Refs. [6,13,14,69–71].
- [56] E. Cadelano, P. L. Palla, S. Giordano, and L. Colombo, Elastic properties of hydrogenated graphene, *Phys. Rev. B* **82**, 235414 (2010).
- [57] E. Cadelano and L. Colombo, Effect of hydrogen coverage on the Young's modulus of graphene, *Phys. Rev. B* **85**, 245434 (2012).
- [58] P. Yadav, B. Khamari, B. Singh, K. V. Adarsh, and A. Agarwal, Fluence dependent dynamics of excitons in monolayer MoSi<sub>2</sub>Z<sub>4</sub> (Z = pnictogen), *J. Phys.: Condens. Matter*, **35**, 235701 (2023).
- [59] S. Sheoran, A. Phutela, R. Moulik, and S. Bhattacharya, Manipulation of valley and spin properties in two-dimensional janus WSiGeZ<sub>4</sub> (Z=N, P, As) through symmetry control, *J. Phys. Chem. C* **127**, 11396 (2023).
- [60] C. H. Lui, K. F. Mak, J. Shan, and T. F. Heinz, Ultrafast photoluminescence from graphene, *Phys. Rev. Lett.* **105**, 127404 (2010).
- [61] D.-H. Kang, H. Sun, M. Luo, K. Lu, M. Chen, Y. Kim, Y. Jung, X. Gao, S. J. Parluhan, J. Ge, S. W. Koh, D. Giovanni, T. C. Sum, Q. J. Wang, H. Li, and D. Nam, Pseudo-magnetic field-induced slow carrier dynamics in periodically strained graphene, *Nat. Commun.* **12**, 5087 (2021).
- [62] K. F. Mak, C. Lee, J. Hone, J. Shan, and T. F. Heinz, Atomically thin MoS<sub>2</sub>: A new direct-gap semiconductor, *Phys. Rev. Lett.* **105**, 136805 (2010).
- [63] M. S. Dresselhaus, G. Dresselhaus, and A. Jorio, *Group Theory: Application to the Physics of Condensed Matter* (Springer Science & Business Media, New York, 2007).
- [64] T. Cai, S. A. Yang, X. Li, F. Zhang, J. Shi, W. Yao, and Q. Niu, Magnetic control of the valley degree of freedom of massive Dirac fermions with application to transition metal dichalcogenides, *Phys. Rev. B* **88**, 115140 (2013).
- [65] M. Mohr, K. Papagelis, J. Maultzsch, and C. Thomsen, Two-dimensional electronic and vibrational band structure of uniaxially strained graphene from *ab initio* calculations, *Phys. Rev. B* **80**, 205410 (2009).
- [66] Q. Zhang, Y. Cheng, L.-Y. Gan, and U. Schwingenschlögl, Giant valley drifts in uniaxially strained monolayer MoS<sub>2</sub>, *Phys. Rev. B* **88**, 245447 (2013).
- [67] A. Priyadarshi, Y. S. Chauhan, S. Bhowmick, and A. Agarwal, Large and anisotropic carrier mobility in monolayers of the MA<sub>2</sub>Z<sub>4</sub> series (M= Cr, Mo, W; A= Si, Ge; and Z= N, P), *Nanoscale* **14**, 11988 (2022).
- [68] S. Aas and C. Bulutay, Strain dependence of photoluminescence and circular dichroism in transition metal

- dichalcogenides: A  $k \cdot p$  analysis, *Opt. Express* **26**, 28672 (2018).
- [69] A. Kormányos, G. Burkard, M. Gmitra, J. Fabian, V. Zólyomi, N. D. Drummond, and V. Fal'ko,  $k \cdot p$  theory for two-dimensional transition metal dichalcogenide semiconductors, *2D Mater.* **2**, 022001 (2015).
- [70] A. Togo, L. Chaput, T. Tadano, and I. Tanaka, Implementation strategies in phonopy and phono3py, *J. Phys.: Condens. Matter* **35**, 353001 (2023).
- [71] Q. Li, W. Zhou, X. Wan, and J. Zhou, Strain effects on monolayer  $\text{MoSi}_2\text{N}_4$ : Ideal strength and failure mechanism, *Phys. E* **131**, 114753 (2021).